Chemical Senses Advance Access published December 14, 2005

Chem. Senses doi:10.1093/chemse/bjj008

Numerical Modeling of Turbulent and Laminar Airflow and Odorant Transport during Sniffing in the Human and Rat Nose

Kai Zhao[1,2], Pamela Dalton[1], Geoffery C. Yang[2,3] and Peter W. Scherer[1,2]

[1]Monell Chemical Senses Center, 3500 Market Street, Philadelphia, PA 19104, USA, [2]Department of Bioengineering, University of Pennsylvania, RM 120, Hayden Hall, 3320 Smith Walk, Philadelphia, PA 19104, USA and [3]Affymetrix, Inc., 3380 Central Expressway, Santa Clara, CA 95051, USA

Correspondence to be sent to: Peter W. Scherer, Department of Bioengineering, University of Pennsylvania, RM 120, Hayden Hall, 3320 Smith Walk, Philadelphia, PA 19104, USA. e-mail: scherer@seas.upenn.edu

Abstract

Human sniffing behavior usually involves bouts of short, high flow rate inhalation (>300 ml/s through each nostril) with mostly turbulent airflow. This has often been characterized as a factor enabling higher amounts of odorant to deposit onto olfactory mucosa than for laminar airflow and thereby aid in olfactory detection. Using computational fluid dynamics human nasal cavity models, however, we found essentially no difference in predicted olfactory odorant flux (g/cm^2 s) for turbulent versus laminar flow for total nasal flow rates between 300 and 1000 ml/s and for odorants of quite different mucosal solubility. This lack of difference was shown to be due to the much higher resistance to lateral odorant mass transport in the mucosal nasal airway wall than in the air phase. The simulation also revealed that the increase in airflow rate during sniffing can increase odorant uptake flux to the nasal/olfactory mucosa but lower the cumulative total uptake in the olfactory region when the inspired air/odorant volume was held fixed, which is consistent with the observation that sniff duration may be more important than sniff strength for optimizing olfactory detection. In contrast, in rats, sniffing involves high-frequency bouts of both inhalation and exhalation with laminar airflow. In rat nose odorant uptake simulations, it was observed that odorant deposition was highly dependent on solubility and correlated with the locations of different types of receptors.

Key words: laminar nasal airflow, odorant uptake modeling during sniff, olfactory odorant uptake, turbulent nasal airflow

Introduction

Many terrestrial vertebrates including humans and rats engage in sniffing behavior to improve olfactory performance by increasing the airflow rate/volume through the nose. However, due to the anatomical complexity of the nasal cavity and high rate and/or frequency of the airflow, detailed study of the impact of sniffing on nasal airflow has not been possible until the development of the computational fluid dynamics (CFD) technique. Computational modeling of fluid flows (CFD) has become a very valuable tool useful for gaining a deeper understanding of biological flows. Flow through the nose in humans or animals is in many ways an ideal system in which to apply this technique since the walls can often be well approximated as rigid, the air as having constant density and viscosity (Newtonian fluid), and the flow as steady or quasi-steady, greatly simplifying the calculations. In the following, we apply the CFD commercial software packages of FLUENT and FIDAP to study the particular cases of airflow and odorant transport during a sniff in humans and rats. Although CFD has previously been applied to study airflow in the rat nose (Kimbell *et al.*, 1993, 1997), it was utilized primarily for the purposes of understanding the deposition pattern and nasal toxicity of various chemical agents and not to evaluate the impact of airflow on olfactory perception. Moreover, very little is known about the potential alterations in airflow in either humans or rats during a sniff. Given that for both rats and humans, sniffing is an integral component of olfactory investigative behavior, it is especially important to determine whether sniffing-induced, turbulent nasal airflow increases olfactory odorant deposition relative to laminar airflow.

The human nose

The initial stages in olfactory perception occur when chemical molecules are transported into the nasal passages via airflow and make contact with olfactory receptor neurons

located in specialized epithelium. Because the majority of the olfactory epithelium is located in a relatively protected area of the nasal passages, during resting breathing, only ~10% of the inspired air reaches this area. In contrast, during sniffing, significantly more odorant-containing air is presumed to reach the olfactory receptor sites and thereby aid in olfactory perception.

Human sniffing behavior usually involves short, high airflow rate (>300 ml/s through each nostril) bouts of inhalation without exhalation in between. At these flow rates, airflow in the nasal cavity is usually turbulent (Hahn *et al.*, 1993). Due to an increase in the pressure drop during sniffing, there is constriction of the nasal valve region, which may intensify turbulence and thus significantly alter nasal airflow to the olfactory region. The occurrence of turbulent flow during sniffing has often been characterized as a factor enabling higher amounts of odorant to deposit onto olfactory mucosa and thereby aid in olfactory detection. Despite this presumption, to date no studies have quantitatively evaluated how sniffing-induced (i.e., turbulent) airflow and resting breathing (i.e., laminar) airflow differentially affect odorant uptake onto olfactory epithelium.

Turbulence is characterized by high-frequency fluctuating velocity components and flow eddies of various sizes throughout the nasal cavity, while laminar flow is smooth and nonfluctuating. It is customary in turbulence modeling to write the instantaneous fluid velocity vector as

$$\vec{U}(\vec{x},t) = \vec{U}(\vec{x}) + \vec{u}'(\vec{x},t), \tag{1}$$

where $\vec{U}(\vec{x})$ represents a time (t)-averaged spatial velocity (x) and u' represents the fluctuating part of the local turbulent fluid velocity. A common measure of the "strength" of turbulence is given by the so-called turbulence intensity

$$I = 100 \times \frac{\sqrt{u'^2_x + u'^2_y + u'^2_z}}{|\vec{U}|}\%, \tag{2}$$

which measures the strength of the fluctuating velocity components and varies from point to point in the flow.

Airflow profiles in human nasal cavities during breathing have been investigated in the past by a number of researchers using *in vitro* models. The earliest nasal physical models were usually cast from noses of human cadavers (Proetz, 1951; Swift and Proctor, 1977; Girardin *et al.*, 1983; Hornung *et al.*, 1987). Quantitative measurement in these casts was made by visualizing smoke in airflow (Proetz, 1951), using miniature pitot tubes (Swift and Proctor, 1977), laser Doppler velocimetry (Girardin *et al.*, 1983), radioactive tracers (Hornung *et al.*, 1987), and particle image velocimetry (Kelly *et al.*, 2000). These experiments, however, made no attempt to quantitatively address the turbulent properties of airflow during sniffing. The only available experimental measurements of turbulence intensity in the human nasal cavity are those obtained by Hahn *et al.* (1993) who studied both laminar and turbulent flows in a 20× scaled anatomically accurate model based on coronal computerized tomography (CT) scan images. Hahn *et al.* found that for resting breathing (1/2 nasal flow rate ~150 ml/s), laminar flow is a good approximation in most of the nose but that for nasal flow rates about twice the resting value and above, fully turbulent flow is a better approximation.

Using Hahn's experimental measurements for validation, Keyhani *et al.* (1995, 1997) developed a finite element numerical model of the right side of the human nasal cavity, obtained from the computerized axial tomography (CAT) scans used by Hahn to construct his large physical model and computed steady-state laminar flow through the model. Of particular interest to olfaction, Keyhani *et al.* studied the effects of the solubility of the odorant in water or mucus, its air phase diffusivity, and the impact of the total nasal airflow rate on the amount and fraction of odorant deposited in the olfactory region. They found that all three of these parameters significantly affected the amount and fraction of odorant deposited. Subramaniam *et al.* (1999) presented a similar model constructed from magnetic resonance imaging scans that included both sides of the human nasal passages and also the posterior nasal airway and nasopharynx. Martonen *et al.* (2002) constructed a three-dimensional (3D) physiologically realistic computer model of the human upper respiratory tract that included both nasal cavities. Their computer representation evolved from cross-sectional slices of a silicone rubber impression of a medical school teaching model of the human head and throat.

Zhao *et al.* followed up on Keyhani's work by developing a rapid meshing procedure starting with CAT scans to compute airflows in the nasal cavities of healthy human subjects (Zhao *et al.*, 2004) and rhinosinusitis patients, who underwent endoscopic surgery (Zhao *et al.*, 2006). They studied the effects of anatomical variations in the nasal valve region and in the olfactory slit on steady-state laminar nasal airflow in the cavity and also computed their effect on olfactory odorant uptake. They found that both laminar flow patterns (streamlines or pathlines) and olfactory odorant uptake were very sensitive to changes in nasal valve geometry.

Due to the complexity of simulating turbulent airflow, all early CFD models of the human nasal cavity evaluated only laminar airflow, which best simulates resting breathing. A preliminary simulation of turbulent airflow was carried out by Lindemann *et al.* (2004) in a recent study, but they did not compare their results to a laminar flow simulation. Moreover, their study only focused on nasal heat exchange but not on mass exchange or olfaction.

In this study, we focused the CFD investigation of the effects of airflow and odorant physicochemical parameters on olfactory odorant deposition using several turbulent models, in addition to laminar airflow, in order to quantify how odorant mass transport onto olfactory epithelium is affected differentially in both flow conditions.

Methods

A 3D anatomically accurate finite volume nasal model (Zhao *et al.*, 2004) constructed from an axial CT of a healthy adult female (1-mm slices, 512×512 pixels, pixel size = $1.0 \times 0.3906 \times 0.3906$ mm) that includes both sides of the human nasal cavity and the nasopharynx was used in this study. In this particular nose, the left nasal valve airway was found to be partially obstructed due to the nasal cycle, which resulted in higher nasal resistance in the left than on the right side. We also included one modified model from Zhao *et al.* (2004) that reduced the nasal valve region volume to simulate the constriction of the nasal valve during human sniffing.

Inspiratory steady-state laminar and turbulent airflows were modeled with a program to perform finite volume numerical analysis (FLUENT, Fluent Inc., Lebanon, NH) in the two versions of the nasal cavity model. In brief, air was mathematically drawn into or out of the nostrils by an imposed pressure drop of either 15 or 160 Pa between the nostrils and the posterior nasopharynx. The magnitude of the pressure drops was determined to ensure that the resulting nasal airflow rates in all nose models were in the range of resting breathing, when the nasal airflow is mostly laminar and of moderate sniffing, respectively (Hahn *et al.*, 1993; Keyhani *et al.*, 1995).

In turbulent flow as noted above, the flow variables of velocity, pressure, odorant concentration, etc., are modeled as containing a time-averaged plus a fluctuating part as for the air velocity given by equation (1) above. This form of the variables is introduced into the governing equations for the conservation of mass, momentum, and energy, which results in terms containing the fluctuating quantities, terms containing the time-averaged quantities, and terms containing both. The result is that there are more variables than there are equations which create the so-called ''closure problem.'' At present, this problem is handled by introducing various ''models'' of the exact equations in which the fluctuating terms are related to the time-averaged terms in various ways, and extra equations are derived to attain mathematical closure. In cases where the turbulent flow occurs within walls, as in the nasal cavity, additional modeling must be done near the wall to allow for the transition to laminar flow in the viscous sublayer next to the wall. The commercial software package, FLUENT, contains several of these turbulence models, and we are employing the relatively new k–ω model (two equations), the k–ε model (two equations with special low-Re treatment), and the Spalart–Allmaras model (one equation) which have been found to give good results for relatively low-Reynolds number turbulent flows contained within walls. The variables k, ω, ε, and μ_t (for Spalart–Allmaras model) refer to the fluctuating quantities of turbulent kinetic energy (k), turbulent dissipation rate (ω and ε), and turbulent viscosity (μ_t), equations for which are derived to attain closure of the models. Finally, it must be said that computational turbulent flow modeling is much more of an art (e.g., in the choice of the best closure model) than is laminar flow modeling, and consequently it is advisable to have experimental data available for comparison with the calculated results.

Results

Figure 1 shows the computed inspiratory laminar and turbulent velocity magnitude (m/s) contours on the coronal cross section in the nasal valve (Figure 1A) and olfactory region (Figure 1C) of the nasal model for a healthy adult female. Comparison between the laminar and various turbulent models at moderate-sniffing airflow rates revealed surprisingly little difference in the airflow pattern in both regions. The laminar model simulation at moderate sniffing airflow rates forces the CFD solver to treat the flow as laminar. Even the laminar simulation at resting breathing (Figure 1B) shows a remarkably similar airflow profile although at a much lower magnitude as that seen during sniffing. The result shown is without taking into account the nasal valve constriction during sniffing.

Figure 2 shows computed turbulent and laminar inspiratory pathlines during resting breathing and moderate sniffing. Under turbulent flow, the pathlines are tangent to the time-averaged velocity vectors, $U(x)$. The pathlines plots (Figure 2A) reveal many more regional differences between the laminar and various turbulent models than the previous contour plots, but in general, the patterns are quite consistent. The plot (Figure 3D) also shows greater difference in airflow pattern during restful breathing. The obstruction found in the left nasal valve region causes significantly different airflow patterns and rates between the right (Figure 2B) and left side, which extends the findings by Zhao *et al.* (2004) for resting breathing conditions. Artificial constriction on the left side (Figure 2C) dramatically changes the airflow pattern, which suggests that for more accurate modeling of nasal airflow during sniffing, it will be necessary to include the fully unsteady dynamics of the nasal valve constriction, although the anatomical details of this are not yet well quantified. Airflow at lower flow rate (rest breathing) shows somewhat similar but less intense patterns (Figure 2D).

Figure 3 shows plots of computed turbulent intensity in a coronal section containing the nasal valve region and the olfactory region. Compared with the nasal valve region, turbulent intensity in the posterior portion of the nasal cavity is less prominent. Although the computed turbulent intensities are generally higher than those measured experimentally by Hahn, the regions of high and low intensity correlate well between the computation and the measurements.

Based on the airflow field that has been generated, the steady-state laminar and turbulent inspiratory odorant transport through airflow and mucosal wall uptake was then simulated using the estimated physiochemical properties in both air phase and in human mucosa (Kurtz *et al.*, 2004;

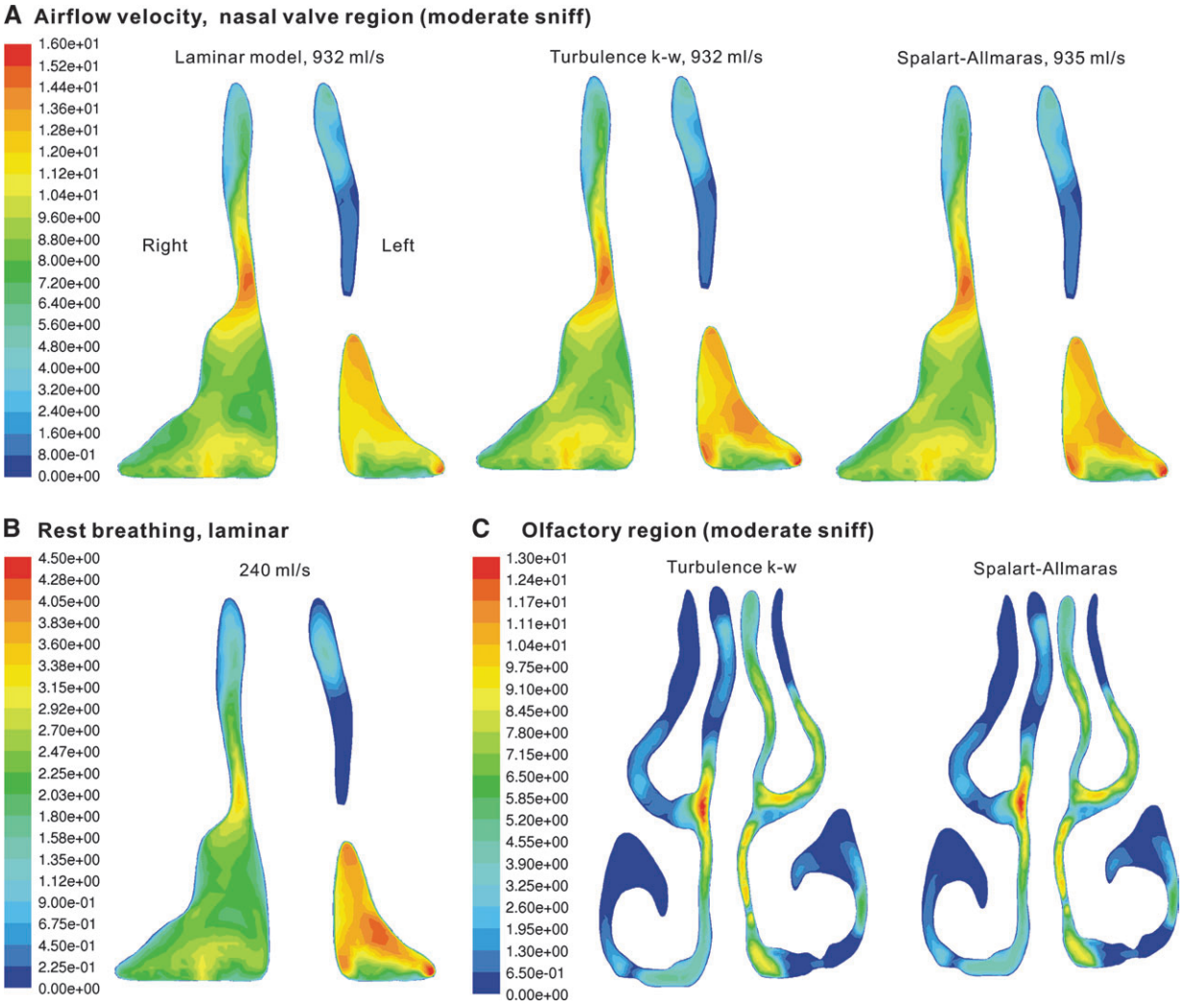

Figure 1 Contour plots of computed inspiratory airflow velocity magnitude (m/s) on the coronal cross section of **(A)** the nasal valve region, with a comparison between laminar and two turbulence models for a pressure drop of 160 Pa between the nares and distal end of nasopharynx, corresponding to a moderate sniff of 930s ml/s bilaterally; **(B)** the nasal valve region for a pressure drop of 15 Pa with a restful breathing of 240 ml/s bilaterally; and **(C)** the olfactory region with the same sniff rate as (A). Note the anatomical obstruction in left nasal valve region in this subject, flow is into the plane of paper.

Zhao *et al.*, 2004) to investigate how different conditions of airflow can differentially affect the transport of odorant to olfactory receptor sites. Figure 4 is a graph summarizing computed odorant uptake over the olfactory mucosa for both sides of the nasal cavity for laminar and turbulent flows for three odorants of different mucosal solubility and air phase diffusivity and for a constricted and unconstricted nasal valve region. The simulations were based on airflow rates at four pressure drops (30, 60, 100, and 160 Pa), which represent the transition from resting breathing to moderate sniffing. The left side consistently has a lower uptake rate than the right due to its constricted nasal valve and higher nasal resistance.

In general, both laminar and turbulent flows at a given flow rate are predicted to have similar uptake flux, which increases only as a function of airflow rate during sniffing. The laminar model would result in slightly more flow than the turbulent model since the turbulent fluctuations yield more pressure drop or more resistance to airflow than in laminar flow. Accordingly, the laminar model would also result in slightly more olfactory mucosal uptake, especially in the constricted left nostril. This outcome is also due to a smoother airflow vortex that brings more local airflow to the olfactory region, which is in contrast to the general expectation that turbulent mixing increases odorant diffusive transport and overcomes the airway constriction. The four symbols within the circle show a comparison of simulations using the same nares–nasopharynx pressure drop simulated by four models: one model for laminar and three models (k–ω, k–ε, and Spalart–Allmaras) for turbulent simulation. In the unobstructed right nostril, a simulated collapsed nasal valve resulted in a significant reduction of olfactory mucosal uptake. This outcome cannot be totally accounted for by the reduction of global nasal airflow

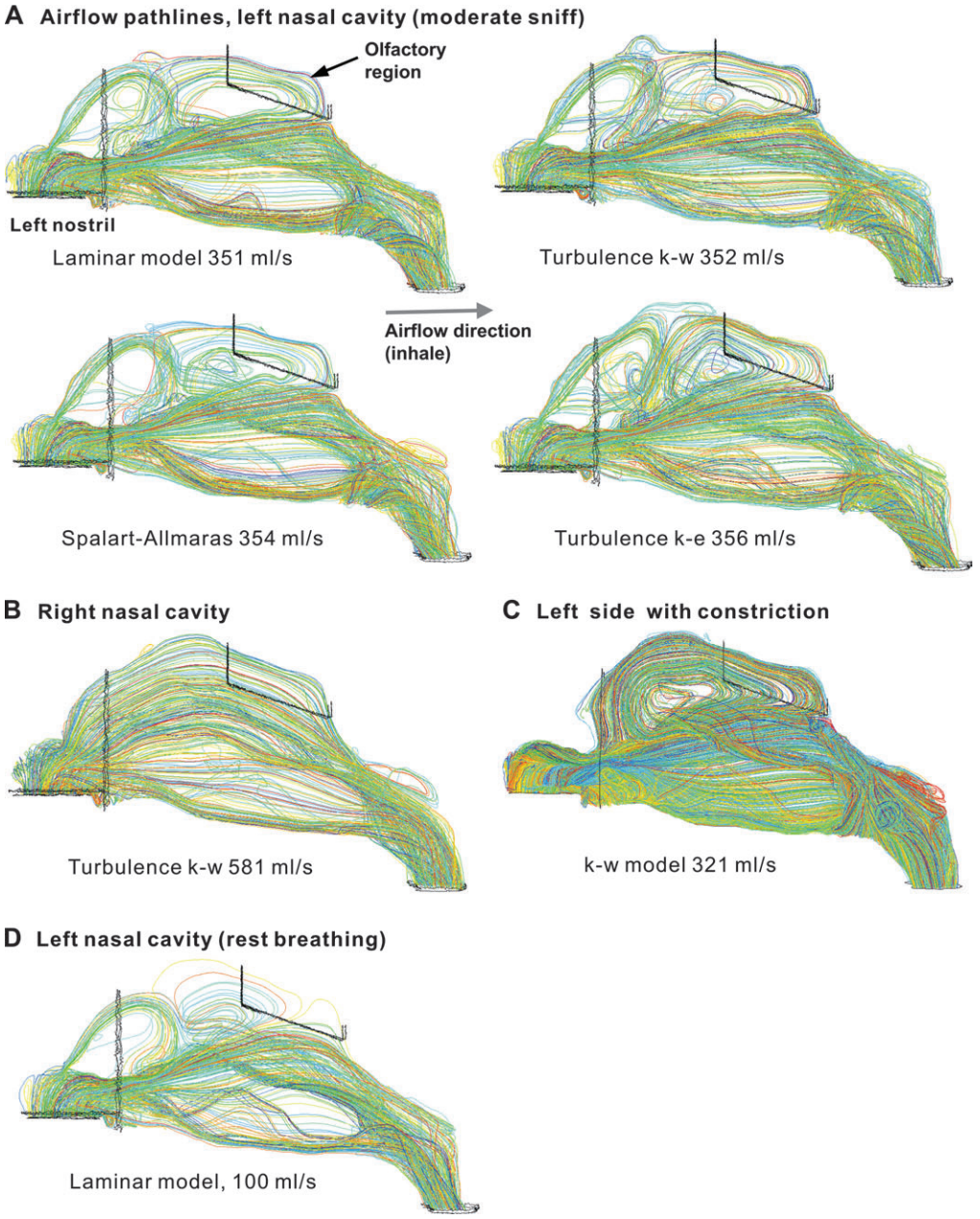

Figure 2 Plots of airflow inspiratory pathlines during moderate sniffing (160 Pa pressure drop), simulated by numerically releasing neutral buoyant particles on the external naris plane and tracing their paths as they flow through the nasal cavity. **(A)** The left and **(B)** the right nasal cavity of the original model, **(C)** the left nasal cavity with imposed constriction of the nasal valve region (Zhao *et al.*, 2004), and **(D)** during rest breathing in the left nasal cavity of the original model. Note dorsal recirculation eddies in left nasal cavity due to nasal valve region obstruction in this subject.

through nostril and is likely due to a redistribution of airflow patterns that direct airflow away from the olfactory region (Zhao *et al.*, 2004) in addition to the increase of nasal resistance as a result of collapsing. It should be noted, however, that in the originally constricted left nostril, the constriction of the nasal valve has less effect on global nasal airflow rate than would be expected. This suggests that the effect of nasal valve collapse during sniffing is not general and may depend largely on the idiosyncratic nasal anatomy.

Olfactory mucosal uptake fluxes of odorants with higher mucosal solubility (*d*-limonene vs. *l*-carvone) and higher air diffusivity (Methanol vs. *l*-carvone) are more affected by the increase in total nasal airflow rate during sniffing. (Data for *d*-limonene is replotted on a side graph with magnified scales.)

The spatial odorant deposition pattern on the olfactory mucosa has been postulated by many researchers to be a determinant of olfactory perception (Mozell, 1966, 1970;

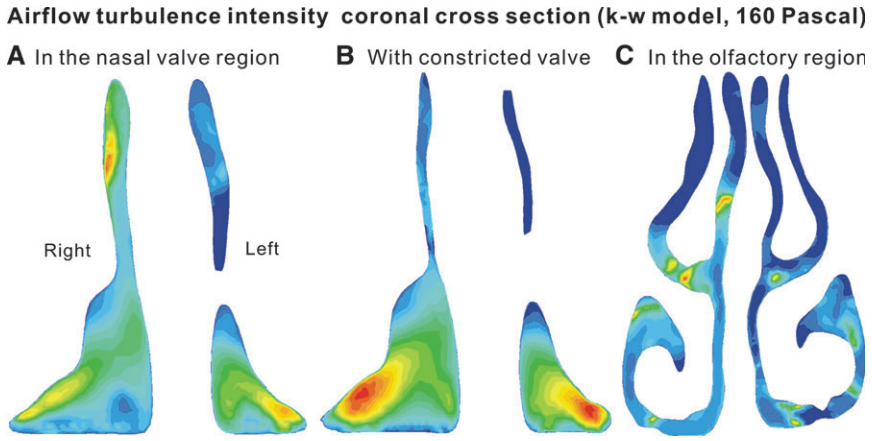

Figure 3 Contour plots of computed airflow turbulence intensity at coronal cross section of the nasal valve and olfactory region simulated by *k*–ω model under total pressure drop of 160 Pa across nares–nasopharynx, corresponding to a moderate sniff (flow rate 930s ml/s bilaterally). Turbulent intensity values (red, highest; blue, lowest) correlated well with experimental measurements of Hahn *et al.* (1993).

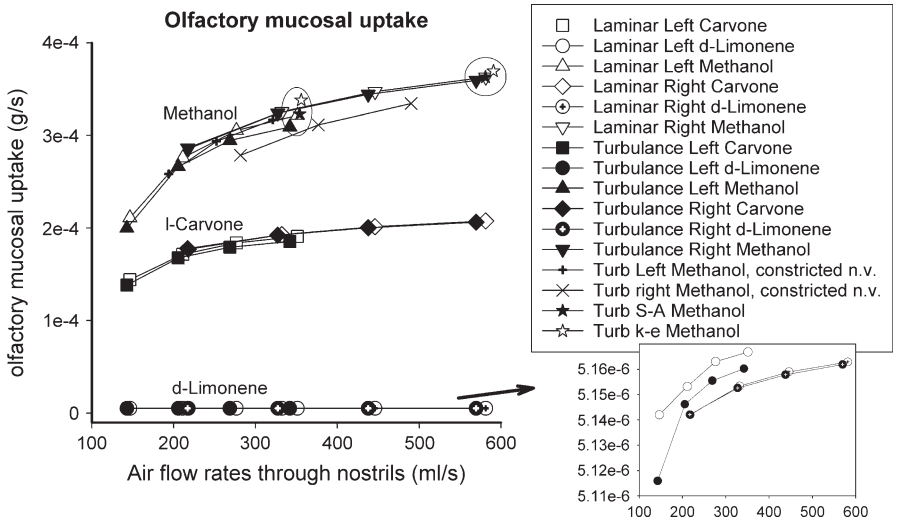

Figure 4 Computed odorant uptake rate (g/s) onto left and right olfactory mucosa using laminar and turbulent (*k*–ω) models in the original and nasal valve constricted nasal cavity models. In general, both laminar and turbulent flows at a given flow rate are predicted to have similar uptake flux, which increases only as a function of airflow rate during sniff. The four symbols within the circle show a comparison of four models (laminar, *k*–ω, *k*–ε, and Spalart–Allmaras) under the same nares–nasopharynx pressure drop. The left side consistently has a lower uptake rate than the right due to its constricted nasal valve and higher nasal resistance. Odorants with higher mucosal solubility (*l*-carvone and methanol) and higher air diffusivity (methanol) are more affected by the change in nasal airflow rate during sniff. (Data for *d*-limonene is replotted with magnified scales.)

Mozell and Jagodowicz, 1973; Moulton, 1976). Figure 5 shows contour plots of odorant uptake patterns in the right and left olfactory septal mucosal wall at different flow rates as predicted by turbulent and laminar models for two odorants of widely differing mucosal solubility. In general, at high flow rates, the spatial deposition patterns produced by both laminar and turbulent models for methanol are close to identical. The patterns for low mucosal solubility *d*-limonene are also quite similar to that of methanol, although with very little spatial variations (note that the color scale shows only 5% of variations). The patterns for low flow rate are remarkably different, smoother, reflecting the less intense airflow stream. The functional impact of these differences remains unknown.

Figure 6 shows computed cumulative olfactory mucosal deposition for a fixed volume (1000 ml) of odorant inhaled at different flow rates. Higher flow rates resulted in shorter duration of inhalation, thus less total odorant uptake by the olfactory mucosa.

The results shown in Figures 4 and 6 imply that in general, for a given odorant, the amount (g) of odorant absorbed into the nasal olfactory mucosa or the odorant mass flux (g/cm^2 s) is predicted to be about the same for both laminar and turbulent flows at a given flow rate, even for a nasal cavity with

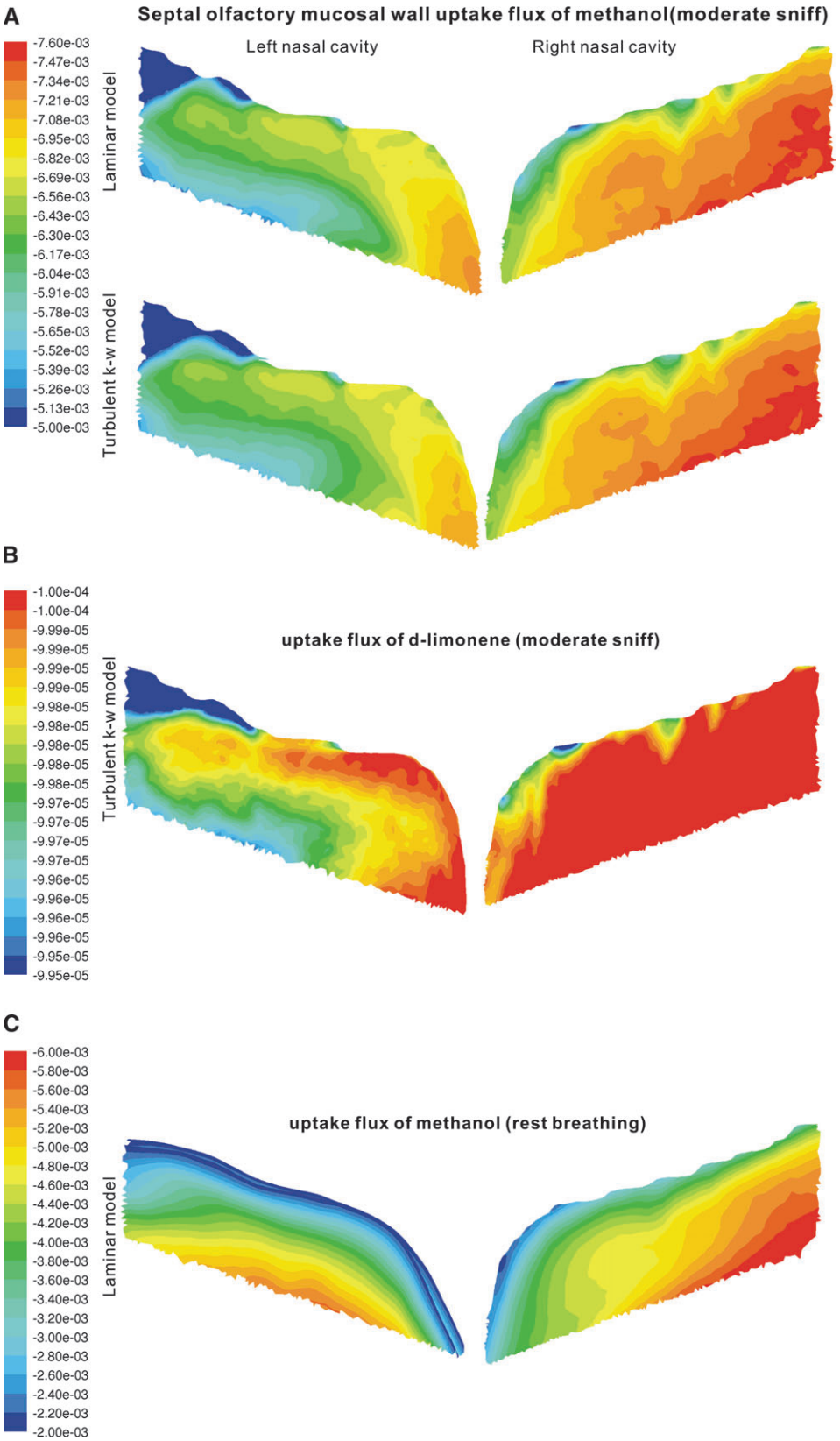

Figure 5 Contour plots of computed mucosal septal wall uptake flux (kg/s·m^2) in the olfactory region during a moderate sniff (160 Pa pressure drop); comparison between left and right nasal cavity; laminar and turbulent (k–ω) models for **(A)** hydrophilic methanol and **(B)** moderately hydrophobic *d*-limonene and **(C)** during rest breathing (15 Pa) for methanol.

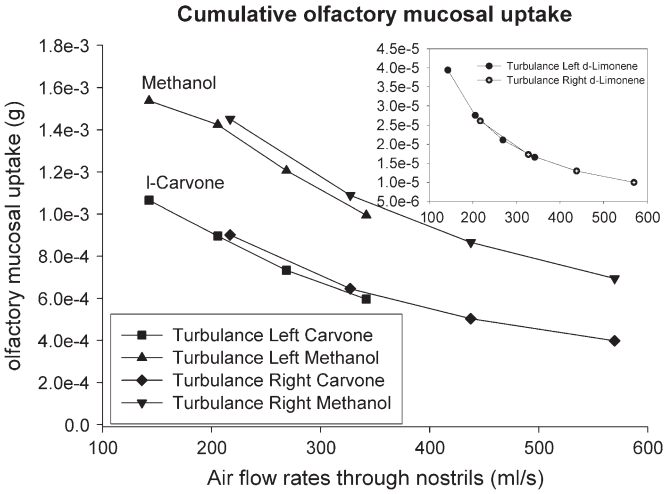

Figure 6 Computed cumulative olfactory mucosal uptake (g) for left and right olfactory regions when the volume of air/odorant mixture inhaled is held fixed at 1000 ml. Higher flow rates represent shorter duration of inhalation, leading to less total odorant uptake by olfactory mucosa.

somewhat constricted nasal valve region. This may seem surprising, but it is understandable when one realizes that the major resistance by far to mucosal absorption occurs in the mucosa and not out in the main stream of the airflow where turbulence occurs. As our simulation indicates, airflow in the human nasal cavity even during sniffing is transitional or low intensity turbulent with a ratio of turbulent viscosity to molecular viscosity less than five (the ratio for a fully developed turbulent airflow is around a few hundreds), thus the increase of eddy diffusivity due to turbulence in the main air stream of the human nasal cavity is limited.

Discussion

To further corroborate our results, one can note that the (equal in steady state) lateral fluxes from the air stream (a) and through the mucosa (m) are given by

$$J_a = K_a \Delta C_a \quad \text{and} \quad J_m = D_w \Delta C_m / \beta H_w 47, \tag{3}$$

where K_a is an air phase mass transfer coefficient (~2–10 cm/s) for laminar or turbulent flow (Hanna and Scherer, 1986; Hanna *et al.*, 1989), D_w is the diffusivity of the odorant in water, β is the dimensionless (C_a/C_m) odorant solubility in water (Keyhani *et al.*, 1995; Kurtz *et al.*, 2004), and H_w is the average depth of the human nasal mucus taken as 30 μm of water (Keyhani *et al.*, 1995). The term H_w/D_w is then adjusted by the empirical correction factor of 47 to represent odorant diffusivity resistance of the entire thickness of the nasal mucosa, the value of which comes from a combination of experiments and numerical simulation on human nasal odorant uptake conducted by (Kurtz *et al.*, 2004).

Dividing the resistances given by equations (3) gives for the ratio of mucosal to air phase lateral mass transfer resistance in the nasal cavity

$$R_m/R_a = \beta K_a 47 H_w/D_w \approx 10 - 1000. \tag{4}$$

The resistance ratio estimate given by equation (4) shows that for both laminar and turbulent airflows in the human nasal cavity, the resistance to lateral odorant mass transfer in the mucosal wall is an order of magnitude or more greater than that in the air phase. This mass flow rate limiting high mucosal wall resistance determines the lateral odorant flux resulting in similar values for both laminar and turbulent airflows since R_m is the same for both.

Figures 4 and 6 show that the most important difference in nasal odorant transport between resting breathing and sniff in humans is the increase in airflow rate and the subsequent increase in odorant uptake flux to the nasal/olfactory mucosa. Figure 6, however, shows that cumulatively, lower flow rates and longer flow durations do lead to more total uptake in the olfactory region for a fixed inspiratory volume (1000 ml per sniff, Sobel *et al.*, 2000). This effect was also found by Keyhani *et al.* (1997) in their laminar flow study and is confirmed here again for turbulent sniff flow rates. Lower flow rates allow more time for more odorant to be absorbed by nasal/olfactory mucosa for a fixed inhaled volume. Increase in odorant uptake flux during sniff due to turbulence was not found in our calculations as noted above due to the controlling high mass transfer resistance located in the nasal mucosal wall.

To understand how sniffing in humans can enhance olfactory perception, we can hypothesize on the basis of odorant mass transport calculations shown in Figure 6 that sniffing strategy (strength and duration) is an optimization process involving neural temporal integration, task perception, and breathing capacity. Lower sniff flow rates of longer duration lead to more odorant mass deposited for a given volume inspired and result in a longer neural integration time than higher sniff flow rates of shorter duration. Sobel *et al.* (2000) has shown that a flow-restricted nostril can achieve a similar perceptual performance (with longer sniff duration) as a high airflow nostril.

The rat nose

In rats, sniffing involves not just inhalation but also high-frequency bouts of both inhalation and exhalation. Typical physiological values (Youngentob *et al.*, 1987) are as follows: frequency 1.0–8 Hz, external nares hydraulic diameter ~0.18 cm, nasal cavity length ~3.0 cm, and average air velocity in nares, 70–380 cm/s. Using these values gives a range of rat external nares Reynolds number of 100–400 and a range of nasal cavity Strouhal number of 0.3–0.5, both of which suggest laminar and steady flow to be good approximations for sniff modeling in rats. Based on the values of the rat nasal cavity Reynolds number, it is unlikely that turbulent airflow ever occurs there.

The rat nasal airway is much more anatomically complicated than that of humans, especially in the posterior region.

There have been several *in vitro* and CFD approaches to study airflow patterns in the nasal cavities of rodents. Morgan *et al.* (1991) have performed a series of experiments and flow simulations on the F344 rat nasal cavity using water–dye streams flowing steadily in acrylic hollow nasal casts. Kent *et al.* (1996) employed the voltage-sensitive dye technique to study olfactory mucosal neural activity patterns by puffing three odorants with varying solubility directly onto the entire rat olfactory mucosa and also by drawing the odorants at three different flow rates along the mucosal flow path. Kimbell *et al.* (1993, 1997) developed a 3D CFD nasal cavity model of the F344 rat based on coronal step section and numerically reproduced inspiratory airflow stream patterns similar to the experimentally observed one. However, these studies were motivated mostly by toxicological concerns and focused especially in the anterior part of the nasal cavity and on high mucosal solubility reactive pollutants such as formaldehyde.

Using the commercial numerical finite element package FIDAP, we simulated steady, laminar inspiratory and expiratory airflow and odorant transport in the nasal cavity of a Sprague–Dawley rat (Yang, 1999). A polymer cast of the rat nasal cavity was obtained and sectioned horizontally on a milling machine to produce 88 longitudinal sections which were used to construct the finite element mesh. The results of steady-flow streamline calculations and olfactory odorant uptake for a half nasal flow rate (maximal sniff) of 504 ml/min are shown in Figures 7–10.

Figure 7 shows inspiratory streamlines (pathlines) traced out by neutrally buoyant fluid particles released near the medial septal walls at the external nares. The olfactory epithelium is indicated in gray. As can be seen, some inspiratory streamlines enter the olfactory region dorsally then bend ventrally and back toward the external nares before reversing direction again and exiting through the middle part of the pharyngeal tube. These "S-shaped" inspiratory streamlines enter the olfactory ethmoid recesses and carry odorants into the olfactory region. Similar streamlines were found during flow in a rat nasal cast by Morgan *et al.* (1991) and in a finite element numerical model by Kimbell *et al.* (1997).

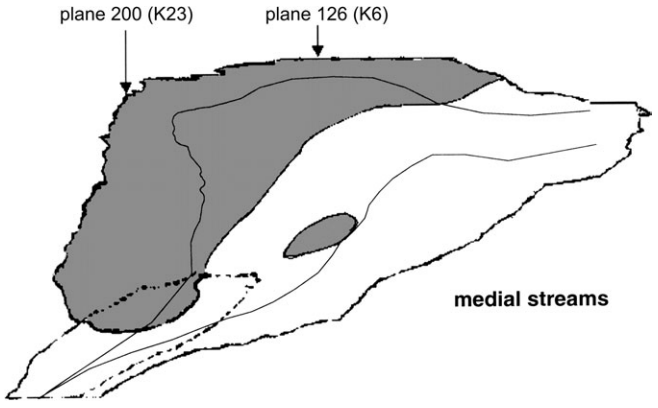

Figure 7 Numerically simulated inspiratory streamline (pathline) trajectories for neutrally buoyant particles released near the medial septal wall of the rat external nares. Note the S shape of the ventral streamline. Olfactory epithelium is shaded in gray. Dashed outline represents boundary of the septal window of the nasopharyngeal meatus. Half nasal flow rate is 504 ml/min. Numbers refer to the location of the coronal plane sections of Yang *et al.* (1999) and those of Kimbell *et al.* (1997). Direction of flow is from right to left.

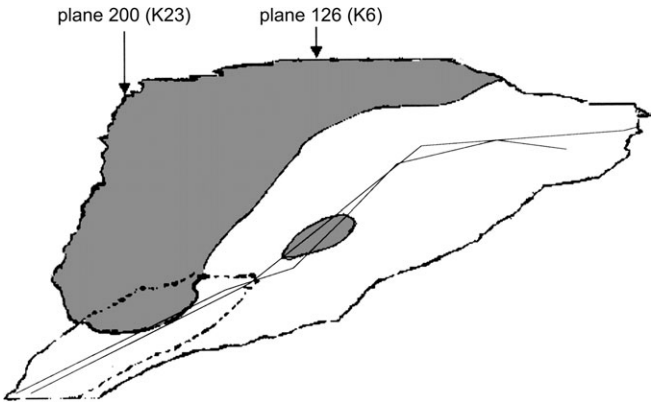

Figure 8 Numerically simulated streamlines (pathlines) for expiratory flow (half nasal expiratory flow rate = 504 ml/min) in the rat nasal cavity. As in Figure 7, medially originated streamlines are shown. Note the lack of S-shaped streamlines. Flow direction is from left to right.

Calculated streamlines for steady exhalatory flow are shown in Figure 8. In general, as can be seen, the exhalatory streamlines do not bend upward and pass through the ethmoid recesses as do the inhalatory streamlines. This lack of reversibility results in a trapping of inhaled air and odorant in the rat olfactory region which is not immediately washed out on exhalation. This trapping phenomenon is likely a very important aspect of the airflow in the rat sniffing strategy and allows odorant to be retained longer in the complex ethmoid air spaces where it can come in contact for a longer time with olfactory receptors on the epithelium. As noted below, the shape of the inspiratory and expiratory streamlines needs to be further tested in a completely unsteady flow calculation.

Figures 9 and 10 show the results of the calculation of odorant uptake on coronal sections of different regions of the rat nose for a maximal sniff inspiratory and expiratory airflow rate of 504 ml/min. Figure 9 shows the calculated uptake results for the highly water-soluble odorant, *l*-carvone, while Figure 10 shows the results for the very water-insoluble octane.

The major result is the finding that the highly soluble odorant *l*-carvone is mostly absorbed dorsally and closer to the septum on both inhalation and exhalation with very little reaching the lateral ethmoid recesses due to the large amount absorbed in the upstream parts of the flow path.

For the insoluble octane, however, much more absorption takes place laterally especially on inhalation due to the S-shaped streamlines and lack of upstream absorption. For

Figure 9 Vector plots of inspiratory uptake of the odorant *l*-carvone (moderately soluble in mucus) on four rat nasal cavity cross sections (Yang numbers 163, 176, 200, 226) left to right, anterior to posterior. Half nasal inspiratory flow rate is 504 ml/min. Reference vector represents 1×10^{-3} g *l*-carvone deposited/cm^2·s. Note medially located deposition. Flow is out of plane of paper.

octane, there is practically no absorption dorsally and medially as for *l*-carvone.

These two patterns of odorant absorption correspond roughly to (Strotmann *et al.*, 1994) zone I (dorsomedial) and zones II and III (lateral) types of receptors, respectively, and imply a structural–functional airflow and odorant detection relationship. Much more study, however, is required to fully investigate the phenomenon.

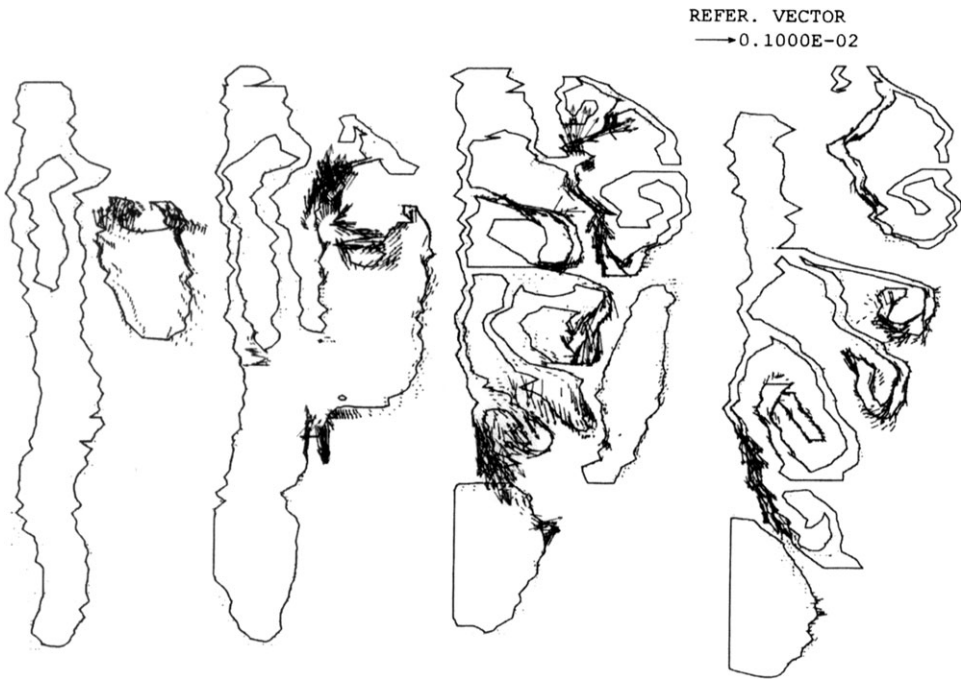

Figure 10 Vector plots of the inspiratory rat nasal cavity uptake of the odorant octane (very insoluble in mucus) for a half nasal flow rate of 504 ml/min. Note the mostly lateral deposition compared to the more soluble *l*-carvone shown in Figure 9. Reference vector represents magnitude of 1×10^{-3} g octane deposited/cm^2·s. Flow is out of plane of paper.

Conclusions

Sniffing behavior in humans produces turbulent airflow through the human nasal passages, and it has been presumed that this type of airflow greatly alters the amount of odorant which reaches the olfactory mucosa. The numerical simulations of human sniffing described above, however, reveal that the odorant mass transport onto the olfactory mucosa during sniffing (turbulent airflow) is remarkably similar to that which occurs during resting breathing (i.e., laminar airflow) if the total flow rate is the same in both conditions. This is due to the very much larger mass transport resistance in the mucosal wall than in the turbulent air stream. In simulating odorant transport in the rat nose, turbulence is never expected to occur, laminar flow modeling is adequate. From the perspective of fluid mechanics, turbulent airflow is less likely to develop in a well-channeled, low–Reynolds number flow region, such as the rat nasal cavity with complex turbinate structure, than in a free stream region, such as a much open airway in human nasal cavity. However, the question remains unsolved as to whether the occurrence of turbulent airflow during sniffing in the human nasal cavity with less-developed turbinate structure than rats is a functional advantage, a disadvantage, or simply irrelevant, given that the major driving force from an evolutionary perspective to develop turbinate structure may be to increase surface area to facilitate heat/mass exchange.

The similarity of computed laminar and turbulent olfactory odorant mass flux means that advantageously, the computationally simpler and faster laminar model can be used for most numerical estimates of olfactory odorant uptake for both resting breathing and sniffing. This outcome will enable the application of these computational techniques for modeling odorant transport for both research and clinical goals.

Despite the progress reported here, limitations to the numerical simulations must be kept in mind, namely, 1) the use of a constant and uncertain depth H_w for the aqueous slab model of the entire nasal mucosa and 2) the uncertainty of the value of odorant molecular diffusivity D_w in the mucosa. These limitations are addressed by the use of the empirical mucosal resistance factor 47 but uncertainty still exists. Moreover, the simulations do not take into consideration the complete unsteady nature of the nasal airflow in both humans and rats but instead model it as a steady airflow.

Completely unsteady calculations remain to be performed, especially for rats, to reveal the extent to which S-shaped streamlines present during inspiration but not expiration may trap odorant in the lateral ethmoid regions and result in longer availability of odorant for olfactory detection. In humans, completely unsteady calculations will be needed to accurately assess the effect of nasal valve region collapse or constriction that occurs during sniff on olfaction.

Until these points can be addressed, the numerical odorant flux simulations must be viewed as very valuable qualitatively correct approximations of sniff but with the understanding that large individual variations may exist. Nevertheless, the ability to accurately model the transport and deposition of volatile chemicals in the nasal passages under both turbulent and laminar airflow conditions is an important tool for predicting the damage from inhaled volatiles and understanding the impact of various rhinological conditions on olfaction.

Acknowledgements

The authors wish to thank Dr Keyvan Keyhani (Asyst Technologies, Inc.) and Dr Shoreh A. Hajiloo (GE Energy, Combustion Technology) for their consultation in CFD modeling. The study was funded by National Institutes of Health grants DC 00220, DC 00072 (to Dr Maxwell M. Mozell, Department of Physiology, College of Graduate Studies, Upstate Medical University, Syracuse, NY), and P50 DC00214 (to P.D.).

References

Girardin, M., Bilgen, E. and **Arbour, P.** (1983) *Experimental study of velocity fields in a human nasal fossa by laser anemometry.* Ann. Otol. Rhinol. Laryngol., 92, 231–236.

Hahn, I., Scherer, P.W. and **Mozell, M.M.** (1993) *Velocity profiles measured for airflow through a large-scale model of the human nasal cavity.* J. Appl. Physiol., 75, 2273–2287.

Hanna, L.M., Frank, R. and **Scherer, P.W.** (1989) *Absorption of soluble gases and vapors in the respiratory system.* In Chang, H.K. and Paiva, M. (eds), Respiratory Physiology. Marcel Dekker Inc., New York, pp. 277–316.

Hanna, L.M. and **Scherer, P.W.** (1986) *Measurement of local mass transfer coefficients in a cast model of the human upper respiratory tract.* J. Biomech. Eng., 108, 12–18.

Hornung, D.E., Leopold, D.A., Youngentob, S.L., Sheehe, P.R., Gagne, G.M., Thomas, F.D. and **Mozell, M.M.** (1987) *Airflow patterns in a human nasal model.* Arch. Otolaryngol. Head Neck Surg., 113, 169–172.

Kelly, J.T., Prasad, A.K. and **Wexler, A.S.** (2000) *Detailed flow patterns in the nasal cavity.* J. Appl. Physiol., 89, 323–337.

Kent, P.F., Mozell, M.M., Murphy, S.J. and **Hornung, D.E.** (1996) *The interaction of imposed and inherent olfactory mucosal activity patterns and their composite representation in a mammalian species using voltage-sensitive dyes.* J. Neurosci., 16, 345–353.

Keyhani, K., Scherer, P.W. and **Mozell, M.M.** (1995) *Numerical simulation of airflow in the human nasal cavity.* J. Biomech. Eng., 117, 429–441.

Keyhani, K., Scherer, P.W. and **Mozell, M.M.** (1997) *A numerical model of nasal odorant transport for the analysis of human olfaction.* J. Theor. Biol., 186, 279–301.

Kimbell, J.S., Godo, M.N., Gross, E.A., Joyner, D.R., Richardson, R.B. and **Morgan, K.T.** (1997) *Computer simulation of inspiratory airflow in all regions of the F344 rat nasal passages.* Toxicol. Appl. Pharmacol., 145, 388–398.

Kimbell, J.S., Gross, E.A., Joyner, D.R., Godo, M.N. and **Morgan, K.T.** (1993) *Application of computational fluid dynamics to regional dosimetry of inhaled chemicals in the upper respiratory tract of the rat.* Toxicol. Appl. Pharmacol., 121, 253–263.

Kurtz, D.B., Zhao, K., Hornung, D.E. and **Scherer, P.W.** (2004) *Experimental and numerical determination of odorant solubility in nasal and olfactory mucosa.* Chem. Senses, 29, 763–773.

Lindemann, J., Keck, T., Wiesmiller, K., Sander, B., Brambs, H.J., Rettinger, G. and **Pless, D.** (2004) *A numerical simulation of intranasal air temperature during inspiration.* Laryngoscope, 114, 1037–1041.

Martonen, T.B., Quan, L., Zhang, Z. and **Musante, C.J.** (2002) *Flow simulation in the human upper respiratory tract.* Cell Biochem. Biophys., 37, 27–36.

Morgan, K.T., Kimbell, J.S., Monticello, T.M., Patra, A.L. and **Fleishman, A.** (1991) *Studies of inspiratory airflow patterns in the nasal passages of the F344 rat and rhesus monkey using nasal molds: relevance to formaldehyde toxicity.* Toxicol. Appl. Pharmacol., 110, 223–240.

Moulton, D.G. (1976) *Spatial patterning of response to odors in the peripheral olfactory system.* Physiol. Rev., 56, 578–593.

Mozell, M.M. (1966) *The spatiotemporal analysis of odorants at the level of the olfactory receptor sheet.* J. Gen. Physiol., 50, 25–41.

Mozell, M.M. (1970) *Evidence for a chromatographic model of olfaction.* J. Gen. Physiol., 56, 46–63.

Mozell, M.M. and **Jagodowicz, M.** (1973) *Chromatographic separation of odorants by the nose: retention times measured across in vivo olfactory mucosa.* Science, 181, 1247–1249.

Proetz, A.W. (1951) *Air currents in the upper respiratory tract and their clinical importance.* Ann. Otol. Rhinol. Laryngol., 60, 439–467.

Sobel, N., Khan, R.M., Hartley, C.A., Sullivan, E.V. and **Gabrieli, J.D.** (2000) *Sniffing longer rather than stronger to maintain olfactory detection threshold.* Chem. Senses, 25, 1–8.

Strotmann, J., Wanner, I., Helfrich, T., Beck, A., Meinken, C., Kubick, S. and **Breer, H.** (1994) *Olfactory neurones expressing distinct odorant receptor subtypes are spatially segregated in the nasal neuroepithelium.* Cell Tissue Res., 276, 429–438.

Subramaniam, R.P., Richardson, R.B., Morgan, K.T. and **Kimbell, J.S.** (1999) *Computational fluid dynamics simulations of inspiratory airflow in the human nose and nasopharynx.* Inhal. Toxicol., 10, 91–120.

Swift, D.L. and **Proctor, D.F.** (1977) *Access of air to the respiratory tract.* In Brain, J.D., Proctor, D.F. and Reid, L.M. (eds), Respiratory Defense Mechanism. Marcel Dekker Inc., New York, pp. 63–91.

Yang, C.C. (1999) Numerical Modeling of Odorant Uptake in the Rat and Bullfrog Nasal Cavities (PhD Dissertation). University of Pennsylvania, Philadelphia, PA.

Youngentob, S.L., Mozell, M.M., Sheehe, P.R. and **Hornung, D.E.** (1987) *A quantitative analysis of sniffing strategies in rats performing odor detection tasks.* Physiol. Behav., 41, 59–69.

Zhao, K., Pribitkin, E.A., Cowart, B.J., Rosen, D., Scherer, P.W. and **Dalton, P.** (2006) *Numerical modeling of nasal obstruction and endoscopic surgical intervention: outcome to airflow and olfaction.* Am. J. Rhinol., in press.

Zhao, K., Scherer, P.W., Hajiloo, S.A. and **Dalton, P.** (2004) *Effect of anatomy on human nasal air flow and odorant transport patterns: implications for olfaction.* Chem. Senses, 29, 365–379.

Accepted November 9, 2005